crystals

MDPI

*Article*

# Deformation and Damage Assessments of Two DP1000 Steels Using a Micromechanical Modelling Method

**Niloufar Habibi [1,*], Napat Vajragupta [2] and Sebastian Münstermann [1]**

[1] Integrity of Materials and Structures, Steel Institute, RWTH Aachen University, Intzestr. 1, 52072 Aachen, Germany; sebastian.muenstermann@iehk.rwth-aachen.de
[2] Interdisciplinary Center for Advanced Materials Simulation (ICAMS), Ruhr-Universität Bochum, Universitätsstr. 150, 44801 Bochum, Germany; napat.vajragupta@rub.de
* Correspondence: niloufar.habibi@iehk.rwh-aachen.de

**Abstract:** Damage characterization and micromechanical modelling in dual-phase (DP) steels have recently drawn attention, since any changes in the alloying elements or process route strongly influence the microstructural features, deformation behavior of the phases, and damage to the micromechanisms, and subsequently the particular mechanical properties of the material. This approach can be used to stablish microstructure–properties relationships. For instance, the effects of local damage from shear cutting on edge crack sensitivity in the following deformation process can be studied. This work evaluated the deformation and damage behaviors of two DP1000 steels using a microstructure-based approach to estimate the edge cracking resistance. Phase fraction, grain size, phase distribution, and texture were analyzed using electron backscatter diffraction and secondary electron detectors of a scanning electron microscope and employed in 3D representative volume elements. The deformation behavior of the ferrite phase was defined using a crystal plasticity model, which was calibrated through nanoindentation tests. Various loading conditions, including uniaxial tension, equi-biaxial tension, plane strain tension, and shearing, along with the maximum shear stress criterion were applied to investigate the damage initiation and describe the edge cracking sensitivity of the studied steels. The results revealed that a homogenous microstructure leads to homogenous stress–strain partitioning, delayed damage initiation, and high edge cracking resistance.

**Keywords:** micromechanical modelling; representative volume element; dual-phase steel; damage; edge cracking

check for updates

**Citation:** Habibi, N.; Vajragupta, N.; Münstermann, S. Deformation and Damage Assessments of Two DP1000 Steels Using a Micromechanical Modelling Method. *Crystals* **2021**, *11*, 805. https://doi.org/10.3390/cryst11070805

Academic Editor: Nima Farzadnia

Received: 18 June 2021
Accepted: 8 July 2021
Published: 10 July 2021

## 1. Introduction

Dual-phase steels (DP steels) have been progressively used in automotive structural applications, since they exhibit a good combination of strength and formability. These outstanding properties originate from the microstructure, where hard martensite islands are dispersed within a soft ferritic matrix. Nevertheless, their sensitivity to edge cracking still remains a challenge and hinders their wide application in complex parts [1–4].

Edge cracking appears mostly in advanced high-strength steels during the forming processes as premature cracks initiated at blanked, pierced, or trimmed edges, which cannot be predicted by conventional forming limit strains. During these processes, the sheared edge and shear-affected zone are exposed to severe plastic deformation, leading to damage onset [5–7]. Therefore, a thorough understanding of the effects of microstructural features on local mechanical and damage behaviors are highly required. However, this could be very complicated for multiphase materials, of which complex microstructures with particular characteristics can be produced by altering the chemical composition and manufacturing process. Phase fractions, phase distributions, grain sizes, and mechanical properties of individual phases strongly influence the strain localization process and general damage behavior of the material [8–11]. Although several studies have been carried out to investigate the microstructural deformation and fracture micromechanisms in DP steels [12–15], only few of them correlated the findings with edge crack sensitivity [16,17], especially by using micromechanical modelling [18].

Therefore, the present work aimed to bridge the microstructural features of DP steels to the macroscale mechanical and damage responses of the materials, in order to estimate their edge formability potential. For this purpose, representative volume elements (RVEs) were generated according to the microstructural characteristics, which were obtained by the electron backscatter diffraction (EBSD) method, and the micromechanical behavior of the individual phases assessed by applying the nanoindentation technique along with crystal plasticity (CP) modelling. Finally, damage initiation was predicted through various strain paths, which can happen during shear cutting and hole expansion processes. Herein, the maximum shear stress fracture criterion was used for damage prediction.

## 2. Materials and Methods

This section describes the geometrical algorithm needed for generating a 3D representative synthetic microstructure in detail, and a method for providing the appropriate microstructural and micromechanical properties as the algorithm inputs.

### *2.1. 3D Artificial Microstructure Modelling Method*

In order to construct representative microstructure models for multiphase crystalline materials, a Laguerre–Voronoi tessellation technique was implemented using the power diagram module in the software Voro++ [19,20]. In this technique, a domain was partitioned into convex polygonal regions according to distances between defined seed points and their individual assigned weights. The weights determine the influence of each point on the region of its adjacent points [21], so that they help to properly reconstruct the grain size distribution. Therefore, it was crucial to define the proper number of seed points, their site in the domain, and their weights to create a representative volume element (RVE).

Here, a box was assumed as the spatial domain that defined the RVE structure. The number of required points was defined equal to the number of material grains that were able to occupy the volume of the box. In this regard, the phase fraction, grain size distribution of each phase, and phase distribution were taken into account. Phase fraction and grain size were derived from real microstructural data. The grain size distribution was expressed by a log-normal probability density function (PDF) [22], Equation (1),

$$f(x) = \frac{1}{x\sigma\sqrt{2\pi}} exp\left[-\frac{(lnx - \mu)^2}{2\sigma^2}\right] \tag{1}$$

where $x$ is the measured sample value. The mean and the standard deviation parameters of the corresponding normal distribution of $lnx$ are showed by $\mu$ and $\sigma$, respectively.

Afterwards, the number of grains at a specific grain size for the defined RVE size was calculated using the cumulative distribution function (CDF) based on the parameters obtained from the PDF. However, to ensure that no free space might be left by directly using these data, a modification was employed on the data to attain proper input data. In this regard, the classical theory of geometry, close-packing of equal spheres in a face-centered cubic (FCC) structure, was applied. In this theory, the densest packing density in a three-dimensional space is 0.74. Therefore, instead of assuming a grain with a diameter of $x_i$ occupied the volume of $x_i^3$, it occupied $\sqrt{2}x_i^3$, which is the volume of the FCC structure. Hence, the total volume occupied within the spheres is 0.74 times the size of the RVE. However, a promising strategy of characterizing microstructural features based on neural networks, using experimental data as training data, is being developed by Pütz et al. [23] and Henrich et al. [24].

The distribution of phases was assumed homogenized by applying the random sequential addition algorithm (RSA) [25,26] in 3D space. To reduce computational time, the RVE size was minimized by applying the periodic Voronoi tessellation, which is copying the original germs around the RVE. In order to employ the finite element method (FEM), RVEs were created in Abaqus/2017 along with the required Python scripts. Although, they were meshed elements, using a 3D finite element mesh generator Gmsh 4.2.2. with tetrahedra. The maximum length between two nodes were defined as 1 μm, and the size of the elements could be reduced regarding the size of the created grains. Note that each element represented only one grain. Moreover, the periodic boundary conditions were applied to the constructed RVE using a node-coupling method [27,28] (Figure 1). In this figure, the red system is independent, and the deformation gradient was prescribed, whereas the blue system is dependent and follows the applied deformation. According to an elaborate study on the deformation behavior of the materials, different loading conditions were applied, such as uniaxial tension, biaxial tension, plane strain tension, and shear.

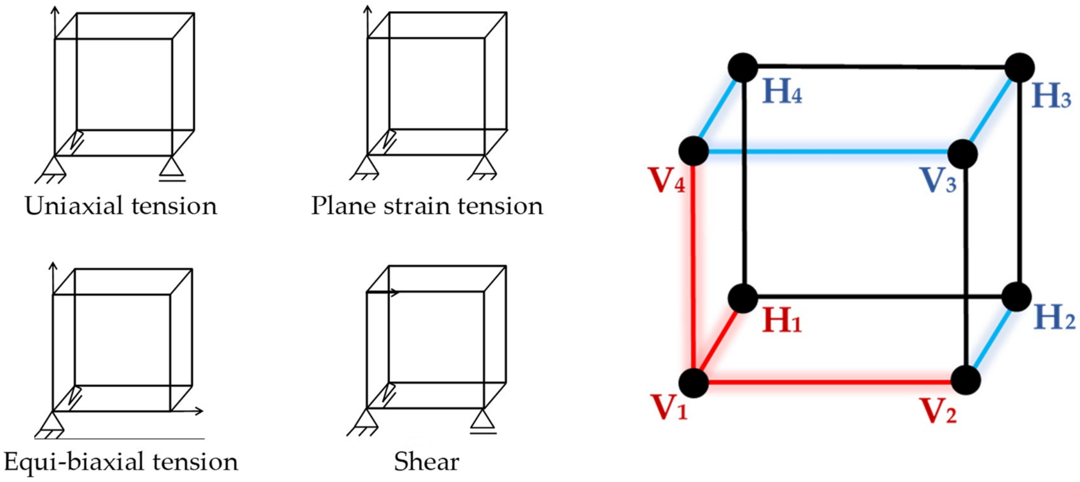

**Figure 1.** Scheme of the applied periodic boundary conditions.

Moreover, in polycrystalline materials, effects of grain orientation and strain hardening are crucial. In this order, the texture features of the materials were also considered. Thus, the orientation distribution function (ODF) was applied to describe the grain orientation distribution using Euler angles, $\varphi = \{\varphi_1, \Phi, \varphi_2\}$. The extracted texture was mapped to the RVEs by performing an iterative process of random assignment of crystallographic orientations to the grains to achieve the desired ODF by minimizing the quantitative differences between the inverse pole figures (IPFs) of the experimental and assigned data. The used MTEX MATLAB scripts for this analysis were taken from References [29,30].

### 2.2. *Material Charaterization as Input Data*

Two different DP1000 grade steels with a thickness of 1.5 mm were investigated. Their chemical compositions are given in Table 1. The phase fractions were determined by analyzing several scanning electron microscopy photos. The grain size and crystallographic texture were characterized using the electron backscatter diffraction (EBSD) method. The analysis was operated on an area of 100 × 100 μm$^2$, at 15 kV, and using a step size of 50 nm.

**Table 1.** Chemical composition of the studied DP1000 steels (wt.%).

| **Materials** | **C** | **Mn** | **Si** | **Al** | **Ti** | **S** | **P** | **Fe** |
|---|---|---|---|---|---|---|---|---|
| CR590Y980T-DP | 0.043 | 1.807 | 0.301 | 0.037 | 0.048 | 0.007 | 0.012 | Bal. |
| CR700Y980T-DP | 0.080 | 2.813 | 0.293 | 0.291 | 0.075 | 0.002 | 0.011 | Bal. |

Since the selected materials were multiphase steels, the hardening behavior of each phase was determined considering the effect of the grain orientation for the ferrite phase and random texture for the martensite phase. Thus, for the ferrite phase, crystal plasticity (CP), modelling a phenomenological constitutive law [31], was used, which is briefly introduced here. This type of model mostly adopts a critical resolved shear stress as a state variable for each slip system. Therefore, the shear rate, $\dot{\gamma}$, is formulated as a function of the resolved shear stress, $\tau$, and the critical resolved shear stress, $\tau_c$. Prominent formulations along these lines were suggested by Rice et al. [32] for metallic crystals. In this framework, the kinetic law on a slip system is as in Equation (2),

$$\dot{\gamma}^{\alpha} = \dot{\gamma}^{0}\left|\frac{\tau^{\alpha}}{\tau_c^{\alpha}}\right|^{\frac{1}{m}} sgn(\tau^{\alpha}) \tag{2}$$

where $\dot{\gamma}^{\alpha}$ is the shear rate on slip system $\alpha$ subjected to the resolved shear stress $\tau^{\alpha}$ at a slip resistance of $\tau_c^{\alpha}$; and $\dot{\gamma}^{0}$ and $m$ are material constants, which describe the reference shear rate and the rate sensitivity of the slip, respectively. The influence of any set of slip system, index $\beta$, on the hardening behavior of a (fixed) slip system $\alpha$ is given as Equation (3),

$$\dot{\tau}_c^{\alpha} = \sum_{\beta=1}^{n} h_{\alpha\beta}\left|\dot{\gamma}^{\beta}\right| \tag{3}$$

where $h_{\alpha\beta}$ is referred to as the hardening matrix in Equation (4).

$$h_{\alpha\beta} = q_{\alpha\beta}\left[h_0\left(1 - \frac{\tau_c^{\beta}}{\tau_s}\right)^{a}\right] \tag{4}$$

Here, $h_0$, $a$, and $\tau_s$ are the slip-hardening parameters, which are considered to be identical for all slip systems as a result of the underlying characteristic dislocation reactions. The parameter $q_{\alpha\beta}$ is related to latent hardening, which is assumed to be 1.0 for coplanar slip systems $\alpha$ and $\beta$ [31,33]. These parameters were calibrated through nanoindentation tests of the ferrite grains and corresponding parallel simulations, by getting the best fit of the load–displacement responses of the material.

The nanoindentation tests were carried out on three relatively large grains on the materials with different grain orientations. For this purpose, a cube-corner indenter tip was chosen for the tests. Each grain underwent three loading rates of 0.1 nm/s, 1 nm/s, and 10 nm/s to reach a 100 nm depth and unloaded with the same speed as the loading. A parallel simulation of nanoindentation was modelled using Abaqus/2017 (Figure 2). The indenter was defined as a discrete rigid of 3 µm in length. A large deformable cube was created to represent a single grain, which meshed with the C3D8 (8-node linear brick) element type with minimum size of 30 nm at the critical area. A frictional coefficient of 0.1 was applied between the contact surfaces using the Coulomb friction model.

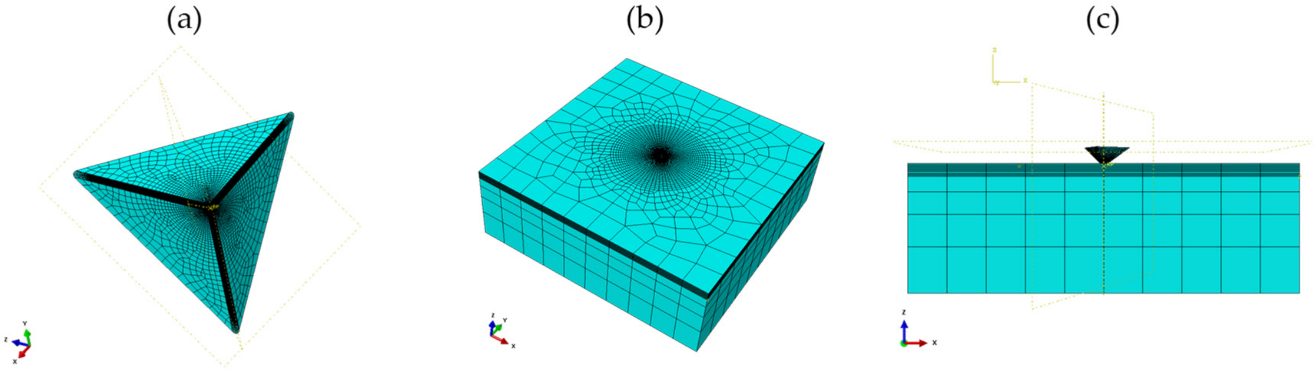

**Figure 2.** 3D nanoindentation model: (**a**) indenter, (**b**) grain, and (**c**) assembly.

Since the martensite grains in the studied materials were very fine, applying nanoindentation tests was impossible. Therefore, the flow curve of this phase was derived by subtracting the flow curve of a fully ferritic RVE under uniaxial tension from the extrapolated flow curve of a conventional uniaxial tensile test of the material. The extrapolation was done using the Hollomon–Voce hardening law [34]. In contrast to the ferrite phase, the deformation behavior of the martensite was considered independent from texture, i.e., isotropic elasticity and J2 plasticity laws were applied.

Moreover, the capability of the micromechanical model in prediction of local damage and edge crack sensitivity was assessed. Thus, the maximum shear stress damage criterion (Tresca) was calibrated for crack initiation in martensite grains at strain of 0.05 [35]. Hence, the damage initiation of the RVEs for different loading conditions were predicted and compared qualitatively to the experimental hole expansion ratio (HER) of the materials. The hole expansion tests were performed with 50° conical punch on shear-cut (with 10% die clearance) and wire-cute holes.

## 3. Results and Discussion

The deformation and damage behavior of the studied DP steels were evaluated using the mentioned micromechanical modelling method. The results are displayed and discussed in the following sections. First, the microstructural and micromechanical features of the materials, which were applied to synthesize the representative volume elements, are shown. Then, the responses of each RVE through different loading conditions are compared and explained.

### *3.1. Synthesis of the 3D Representative Volume Elements*

For generating a microstructural model that can represent the mechanical behavior of materials accurately, defining precise microstructural features, such as the phase fraction, grain size distribution, and texture, are required. Employing the proper mechanical properties in each phase is also vital for a rational study.

#### 3.1.1. Phase Fraction

As expected, the studied dual-phase steels had a ferritic–martensitic microstructure (Figure 3). By analysis of several high-magnification SEM images using Digimizer version 5.6.0 by MedCalc Software Ltd. [36], the fraction of each phase was revealed. CR590Y980T-DP contained 65% ferrite and 35% martensite, and CR700Y980T-DP had 55% ferrite and 45% martensite. Although an EBSD study was carried out in this work, it was not properly capable to distinguish similar crystal structures of the body-centered cubic (BCC) ferrite and body-centered tetragonal (BCT) martensite, especially for these fine microstructures [9].

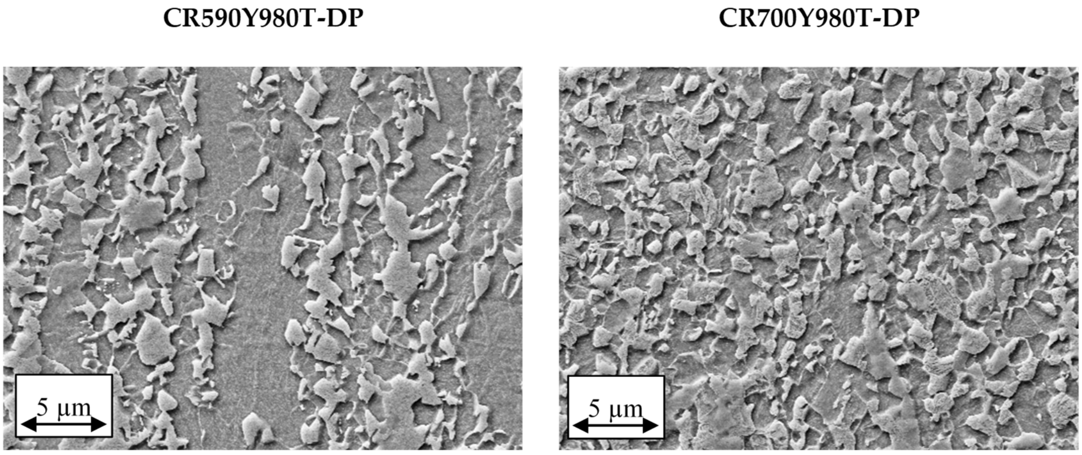

**Figure 3.** The initial microstructure of the studied materials shown in the plane of RD-TD, RD↑ ND→. The brighter and darker grains display the martensite and ferrite phases, respectively.

### 3.1.2. Grain Size Distribution

The grain sizes and their distributions were derived from EBSD images by distinguishing image quality (IQ) values. As shown in Figure 4, the grain sizes of CR590Y980T-DP were clearly coarser than in the other material. The average and maximum grain sizes of the ferrite grains for CR590Y980T-DP were 2.90 and 14.05 µm, while for CR700Y980T-DP, they were 1.76 and 4.53 µm, respectively. The average and maximum grain sizes of the martensite grains for CR590Y980T-DP were 0.69 and 2.34 µm, while for CR700Y980T-DP, they were 0.55 and 2.09 µm, respectively.

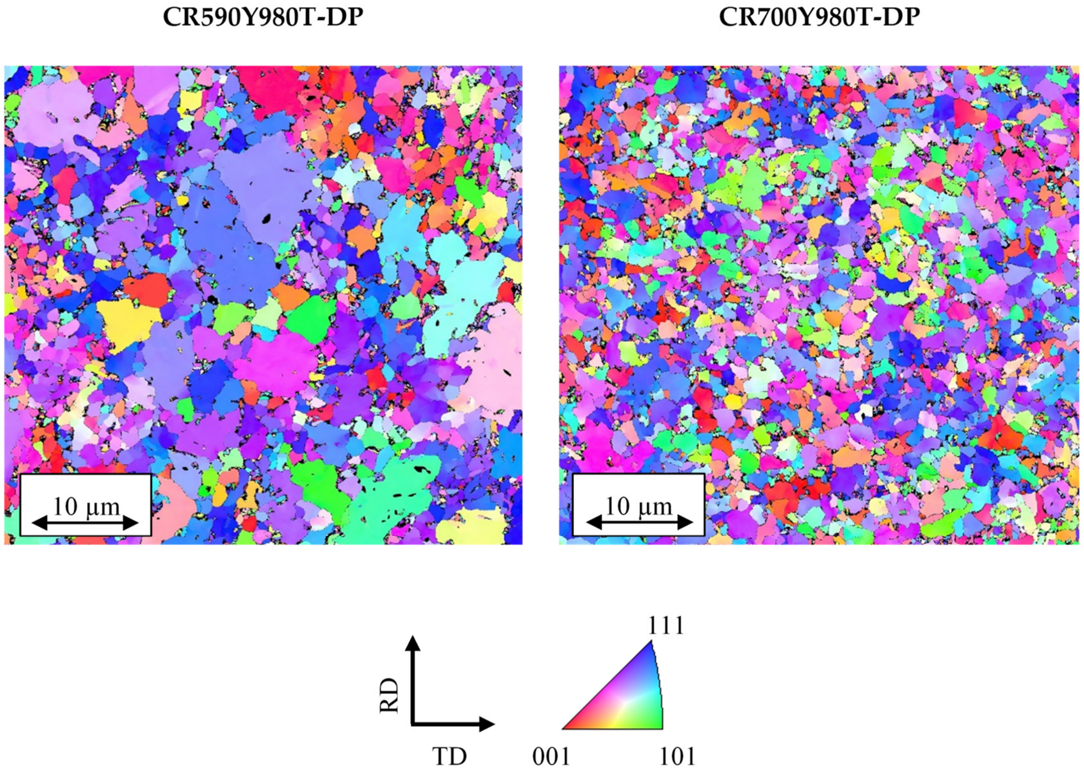

**Figure 4.** EBSD orientation maps for the studies materials on the RD-TD plane, IPF ND.

To construct the grains of the RVEs in a reasonable size range, as explained in detail in the previous section, the statistical frequency of a specific grain size was estimated based on the EBSD data. The log-normal distribution function parameters, mean, and standard deviation of the characterized microstructures were calculated by MATLAB software, (Figure 5). Then, the number of grains in each grain size was determined according to the phase fraction and size of the RVE box of 10 µm × 10 µm × 10 µm (Figure 6). As expected, the number of ferrite grains is lower in CR590Y980T-DP than the other material, 42 grains versus 84 grains, since their grain sizes were also larger, although its ferrite fraction was smaller. The number of martensite grains was also lower for CR590Y980T-DP, as their grain sizes were lower, and also its martensite fraction was lower than the other. In brief, the fine microstructure of CR700Y980T-DP led to create 3.5 times more grains than CR590Y980T-DP. In Figure 6, note that the ferrite grains are represented in different colors, as different crystallographic orientations were required to assign them (which is described later), whereas the martensite grains are only shown in one color, since no texture characteristics were considered for this phase.

**Grain size distribution of ferrite phase**

**CR590Y980T-DP** **CR700Y980T-DP**

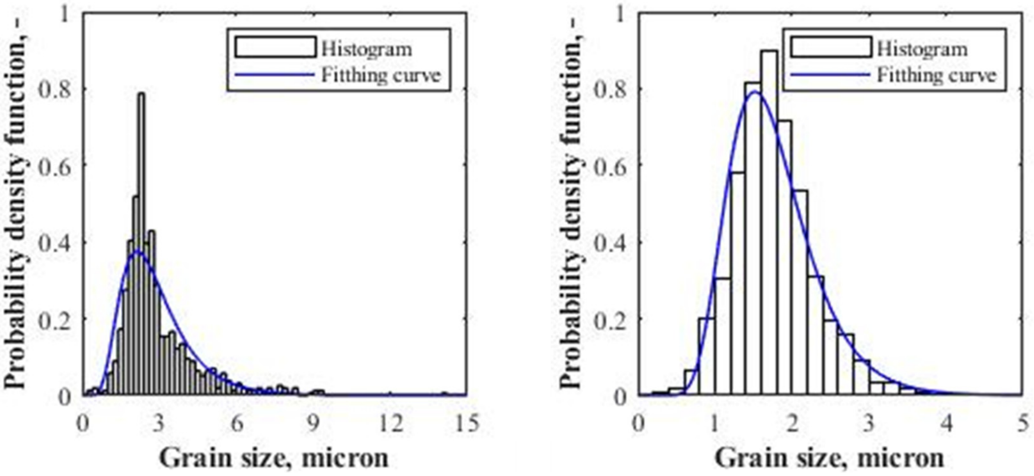

μ = 0.9621
σ = 0.4498

μ = 0.6175
σ = 0.3155

**Grain size distribution of martensite phase**

**CR590Y980T-DP** **CR700Y980T-DP**

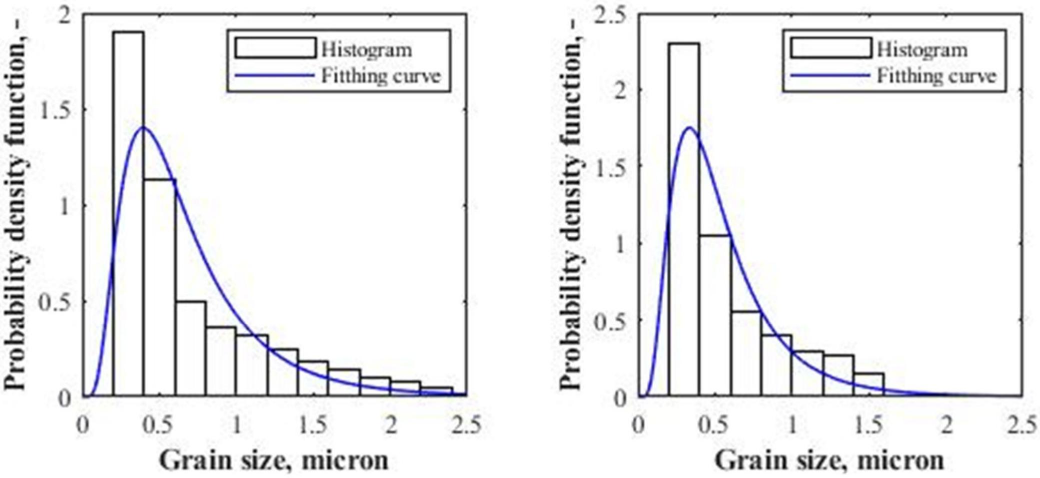

μ = −0.5653
σ = 0.6014

μ = −0.7633
σ = 0.5782

**Figure 5.** Grain size distribution of the ferrite and martensite phases in the studied steels. Parameters of the log-normal distribution function of each histogram were obtained by the best fitting of the curve.

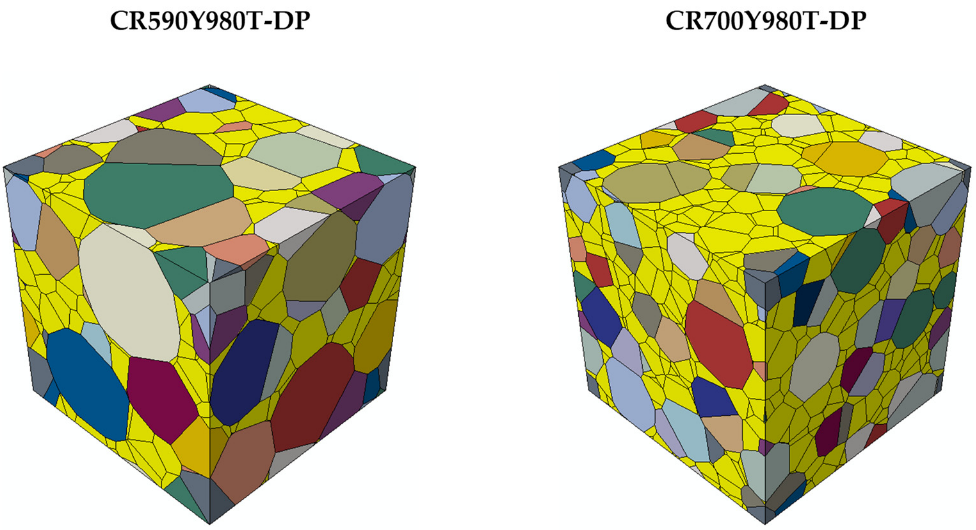

**CR590Y980T-DP** **CR700Y980T-DP**

Number of total grains = 272 Number of total grains = 962

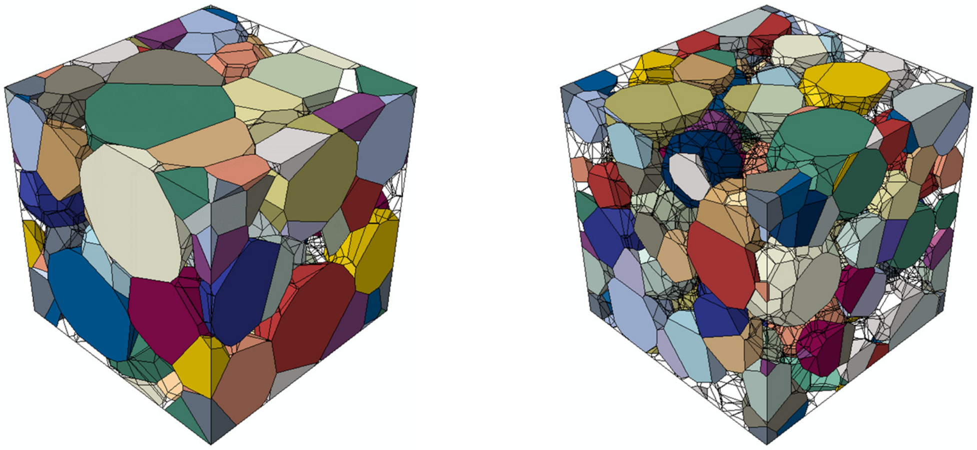

Number of ferrite grains = 42 Number of ferrite grains = 84

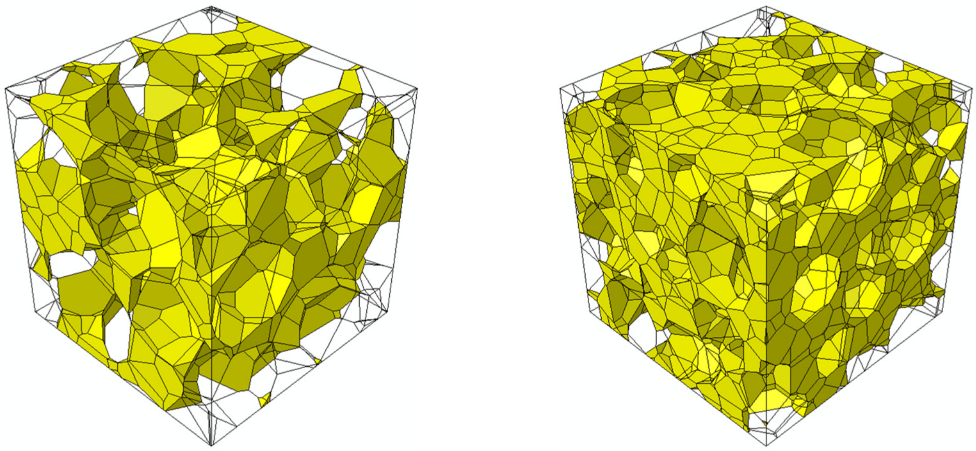

Number of martensite grains = 230 Number of martensite grains =878

**Figure 6.** The generated RVEs (with sizes of 10 μm × 10 μm × 10 μm) for each investigated steel. The grains and number of grains for each phase are shown.

The grain size of the synthesized RVE might be a little bit different from the input data, as the procedure for generating the RVEs is based on randomly placing the seeds. To ensure that the differences were negligible, the grain size distribution of the RVEs for each phase and each material is plotted in Figure 7, as the output histogram. It reveals that for the ferrite phase, the number and range size of the created grains had good agreement with the EBSD data, while for martensite grains, the mean values were higher than the input data. This can happen in this method of RVE generation, since the grains grew and filled the space between spheres, which could cause those grains to grow larger than the assigned weights [22]. Here, this occurrence was observed mostly in martensite grains, as the smaller grains were placed later. Note that the mean sizes of the martensite grains were smaller than the ferrite grains in the studied materials. However, the results were acceptable so far, since the mean size of the martensite grains for CR700Y980T-DP was still higher than CR590Y980T-DP. In addition, for each phase, the mechanical properties' sensitivity to grain size was not considered here; also, the martensite grains usually gathered and formed martensite islands.

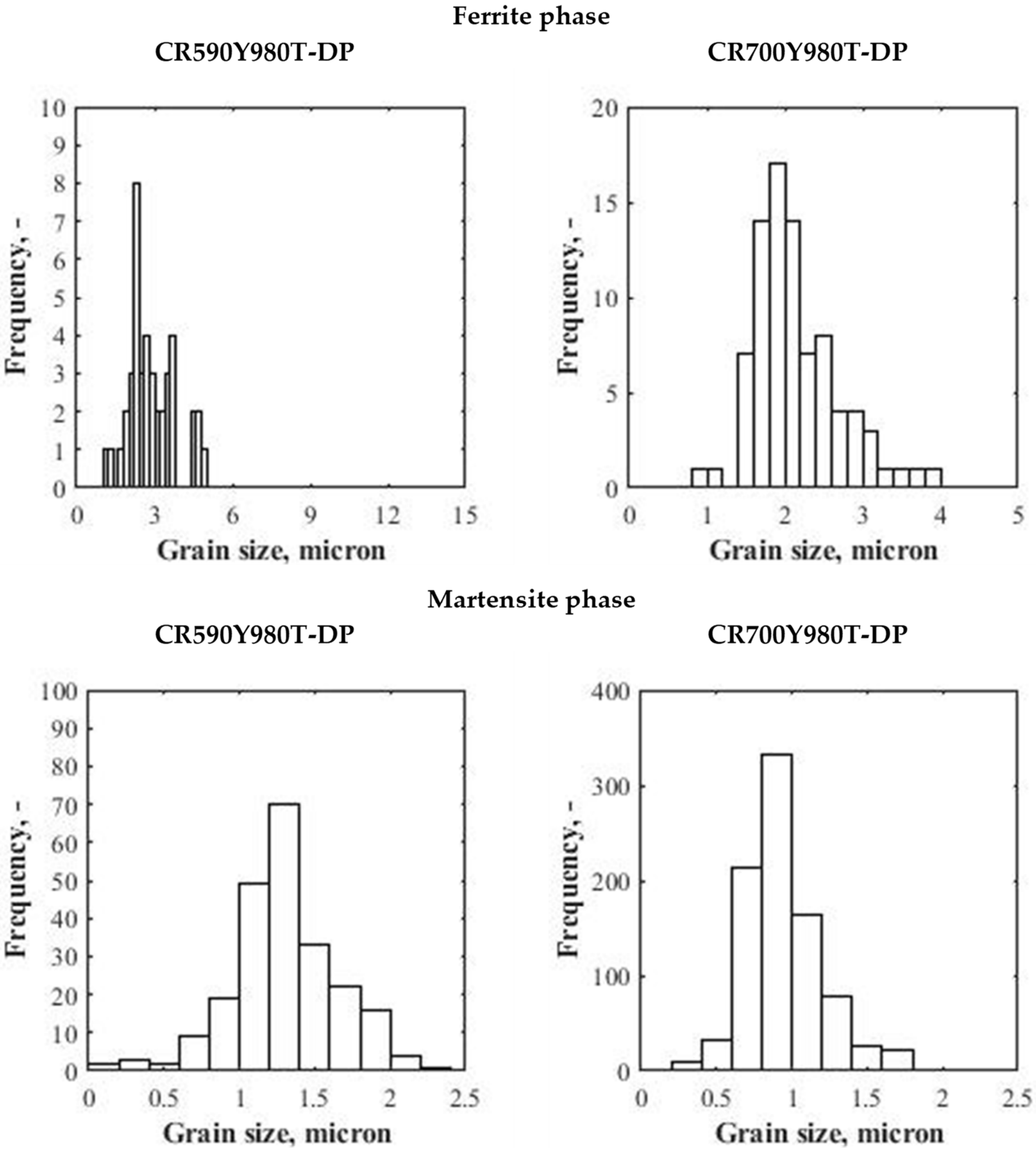
**Ferrite phase**

**CR590Y980T-DP** **CR700Y980T-DP**

**Martensite phase**

**CR590Y980T-DP** **CR700Y980T-DP**

**Figure 7.** Grain size distribution of the ferrite and martensite phases in the generated RVEs.

### 3.1.3. Texture

In the present work, only the effects of ferrite grain texture on the RVE behavior were considered. This assumption was reasonable for the studied steels, as their fine, well-dispersed martensite islands represented a random texture. The crystallographic orientation distributions of the as-received materials and synthesized RVEs are illustrated in Figure 8, in terms of IPFs, which represents acceptable agreement between the data. A relatively higher intensity was observed for the {111} fiber texture, although the overall texture has no significant preferential orientation.

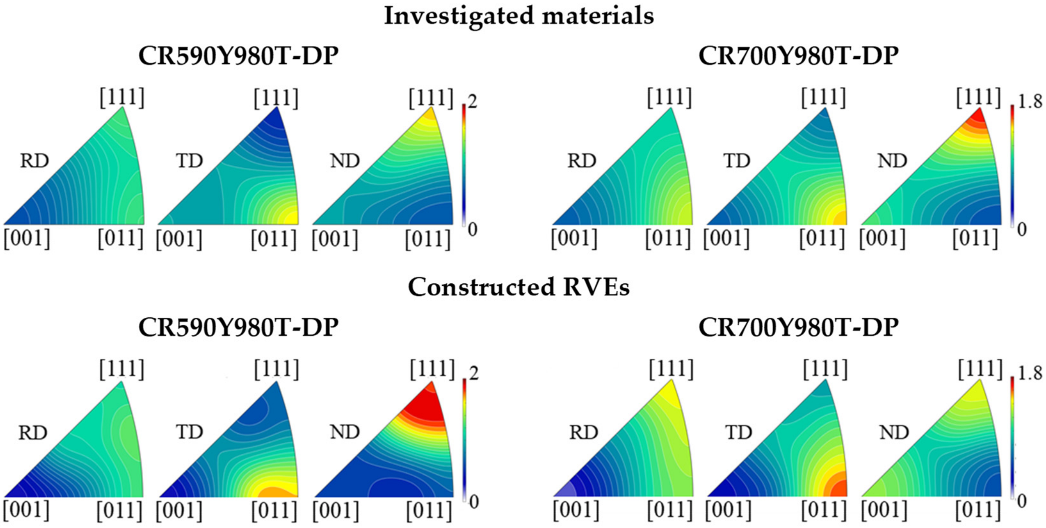

**Figure 8.** Crystallographic orientation distribution of the investigated materials in terms of IPFs.

### 3.1.4. Micromechanical Properties of an Individual Phase

The deformation behavior of the ferrite grains in RVEs were defined using the aforementioned crystal plasticity model for BCC. The parameters were calibrated by performing nanoindentation tests on a single grain and parallel corresponding FEM simulations. The grains with different crystallographic orientations were examined to investigate the effects of grain orientation on their deformation response. The detailed crystallographic information of the tested grains is listed in Table 2. The load–displacement curves and hardness values were extracted from the nanoindentation tests at different loading rates, as seen in Figures 9 and 10, which indicate that the rate and orientation dependencies of the tested grains were low. However, these results could be the consequence of the fine grain size of the studied materials and the applied testing technique. Average hardness values of 2.3 and 2.9 GPa, and a load of 210 µN and 255 µN at 100 nm were measured for CR590Y980T-DP and CR700Y980T-DP, respectively, which noticeably displayed the higher strength of the ferrite phase for CR700Y980T-DP.

**Table 2.** Grain ID and orientation of the test areas.

| Materials | Grain ID | Average Orientation | | |
|---|---|---|---|---|
| | | **φ1** | **Φ** | **φ2** |
| CR590Y980T-DP | 1522 ({111}) | 204.2 | 114.7 | 39.1 |
| | 1355 ({100}) | 148.9 | 69.3 | 20.0 |
| | 1351 ({110}) | 176.1 | 135.5 | 355.1 |
| CR700Y980T-DP | 3198 ({111}) | 19.864 | 50.998 | 311.74 |
| | 1441 ({100}) | 155.55 | 35.663 | 222.51 |
| | 2744 ({110}) | 336.4 | 89.4 | 54.2 |

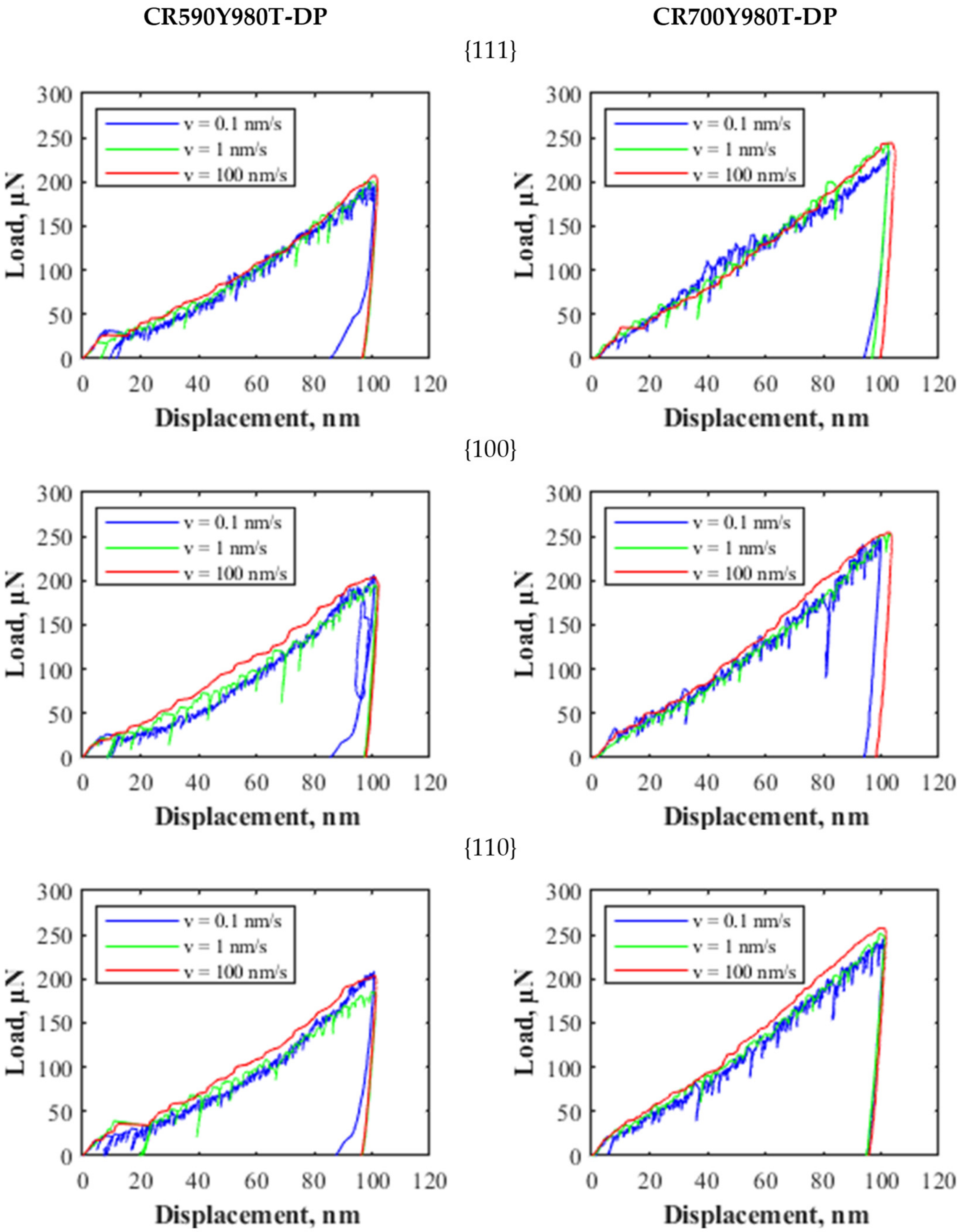

**Figure 9.** Load–displacement curves of the nanoindentation tests at different grains with different loading rates.

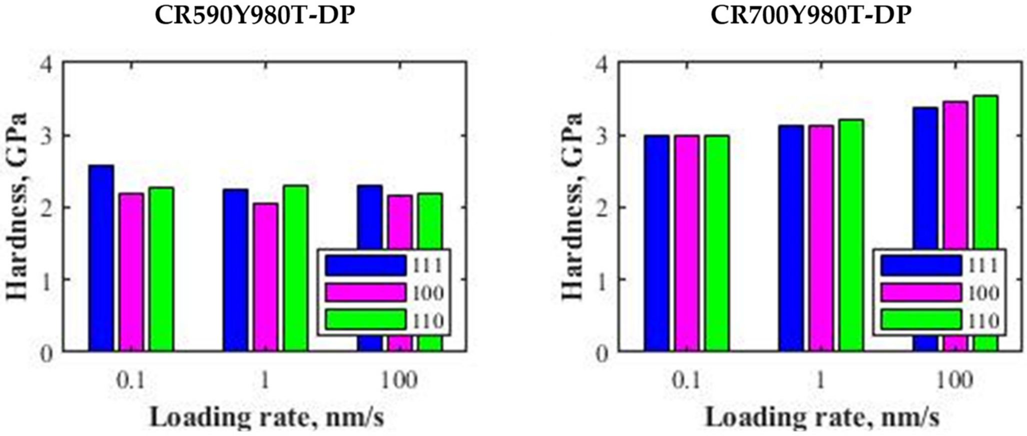

**Figure 10.** The hardness of ferrite grains with different orientations and different loading rates.

The CP parameters were calibrated for the studied steels, by reaching the best fit of the simulated load–displacement curve on the experimental results (Figure 11). The calibrated parameters are listed in Table 3. The number of dislocation slip systems was assumed to be 24, since the slip systems of {110} <111> and {112} <111> are activated at room temperature for BCC. It is worth mentioning, as the nanoindentation tests and the corresponding simulations were not sensitive to loading rate and grain orientation, only one load–displacement curve was available for simultaneous calibration of several CP parameters, which caused the set of parameters for the proper fitting to become non-unique. However, only one set of parameters, as seen in Table 3, could satisfy the assumption of soft ferrite and harder martensite phases; i.e., the flow curve of ferrite should be lower than the tested material. The stress–strain flow curve of the ferrite phase was derived by applying the calibrated CP parameters into uniaxial tension of a single-phase RVE with random texture.

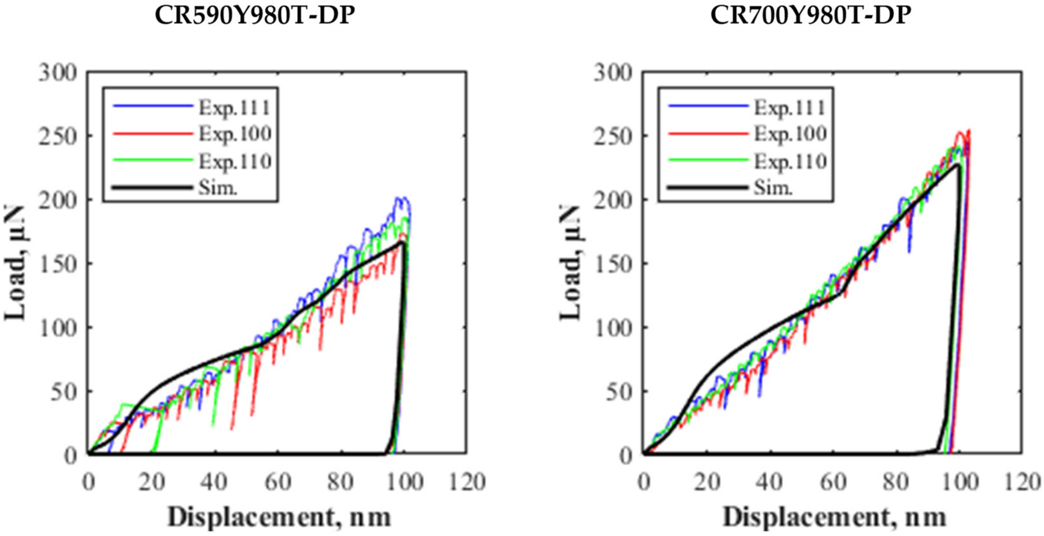

**Figure 11.** The deformation behavior of the calibrated CPFEM ferrite under nanoindentation test shows good agreement with the experimental results.

**Table 3.** Calibrated crystal plasticity parameters of the investigated materials.

| Materials | $c_{11}$ [1] | $c_{12}$ [1] | $c_{44}$ [1] | $\dot{\gamma}^{0}$ [1], 1/s | $\tau_0$, MPa | $\tau_s$, MPa | M [1] | $h_0$, MPa | a |
|---|---|---|---|---|---|---|---|---|---|
| CR590Y980T-DP | 230.1d5 | 134.6d5 | 116.6d5 | 0.001 | 100 | 400 | 0.05 | 1000 | 4 |
| CR700Y980T-DP | 230.1d5 | 134.6d5 | 116.6d5 | 0.001 | 200 | 400 | 0.05 | 1000 | 4 |

[1] The parameters were taken from Reference [37].

Since the martensite grains were very fine, using nanoindentation tests was impossible for these microstructural constituents. Therefore, the mechanical properties of the martensite grains were calculated by subtracting the flow curve of the ferrite phase from the flow curve of the DP steel, based on the fraction of each phase. The flow curves of the ferrite and martensite phases are plotted in Figure 12. Note that a large range of strain is always required to apply in FEM simulations for elaborated studies; however, a maximum strain of only 0.12, through homogeneous deformation of the tensile tests, was achievable for the studied materials. Thus, the Hollomon–Voce hardening law was calibrated for the quasi-static uniaxial tensile test and extrapolated to the large strains in the DP steels' flow curves (Table 4). As mentioned before, the effects of texture on deformation were not considered for the martensite phase, hence only isotropic elasticity and J2 plasticity laws were employed to describe the mechanical properties of martensite.

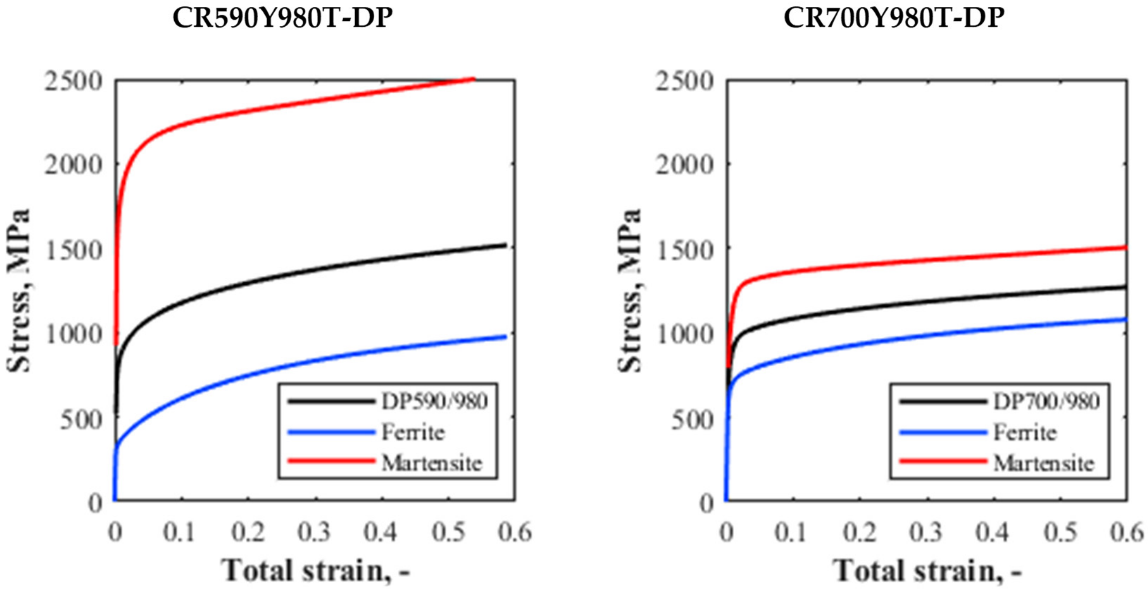

**Figure 12.** The stress–strain flow curve of the materials and their individual phases.

**Table 4.** Fitted parameters of the Hollomon–Voce hardening law.

| Materials | Hollomon–Voce Hardening Law |
|---|---|
| CR590Y980T-DP | $1121.5\,(\varepsilon_p)^{0.2} + 525.4$ |
| CR700Y980T-DP | $474.7\,(\varepsilon_p)^{0.4} + 189.9\,\exp(-177.2\varepsilon_p) + 861.1$ |

Figure 12 shows that the stress–strain behaviors of the materials were in the same range for low strains, such as 0.1, but they vary at larger strains. The level of the flow curves for ferrite in CR590Y980T-DP was lower than in CR700Y980T-DP, especially the yield stress. In contrast, for the martensite phase, the level of the flow curve in CR590Y980T-DP was significantly higher than in CR700Y980T-DP. For instance, the initial yield stresses for the ferrite phases were 301 and 601 MPa and for the martensite phases were 922 and 793 MPa, respectively, for steels CR590Y980T-DP and CR700Y980T-DP. In brief, the flow curves of the different phases are so close for CR700Y980T-DP, whereas in CR590Y980T-DP the flow curves of the phases are quite different. These differences are also visible in the hardness results (Figure 13). The macro Vickers hardness of CR590Y980T-DP was higher than the other materials, 3.4 versus 3.2 GPa, while the hardness of the ferrite phase for CR590Y980T-DP was much lower. Thus, a harder martensite phase could be expected for CR590Y980T-DP. To sum up, the strength levels of ferrite and martensite were closer in CR700Y980T-DP than in CR590Y980T-DP.

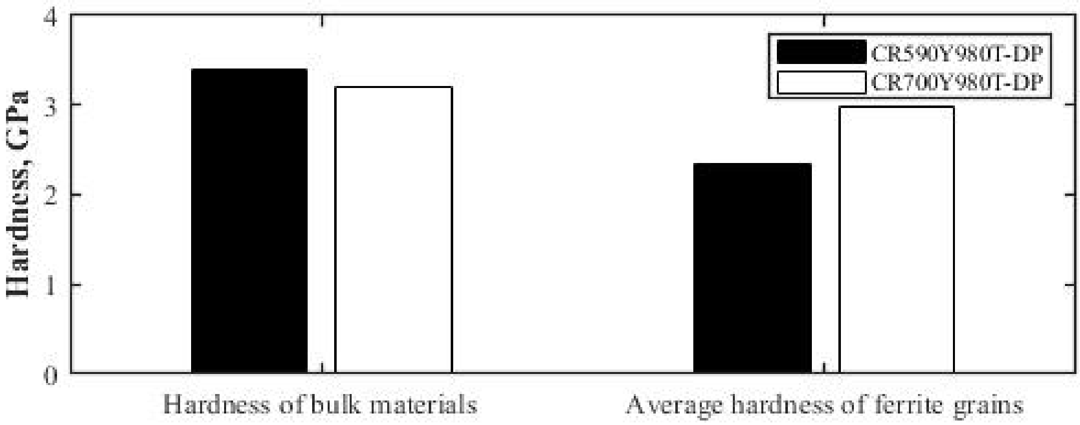

**Figure 13.** The comparison of hardness of the DP steels and their ferrite grains.

The meshed RVEs are displayed in Figure 14. Since CR700Y980T-DP contained finer grains, the number of total elements was higher than the RVE of the other material, 101,799 versus 42,487 elements.

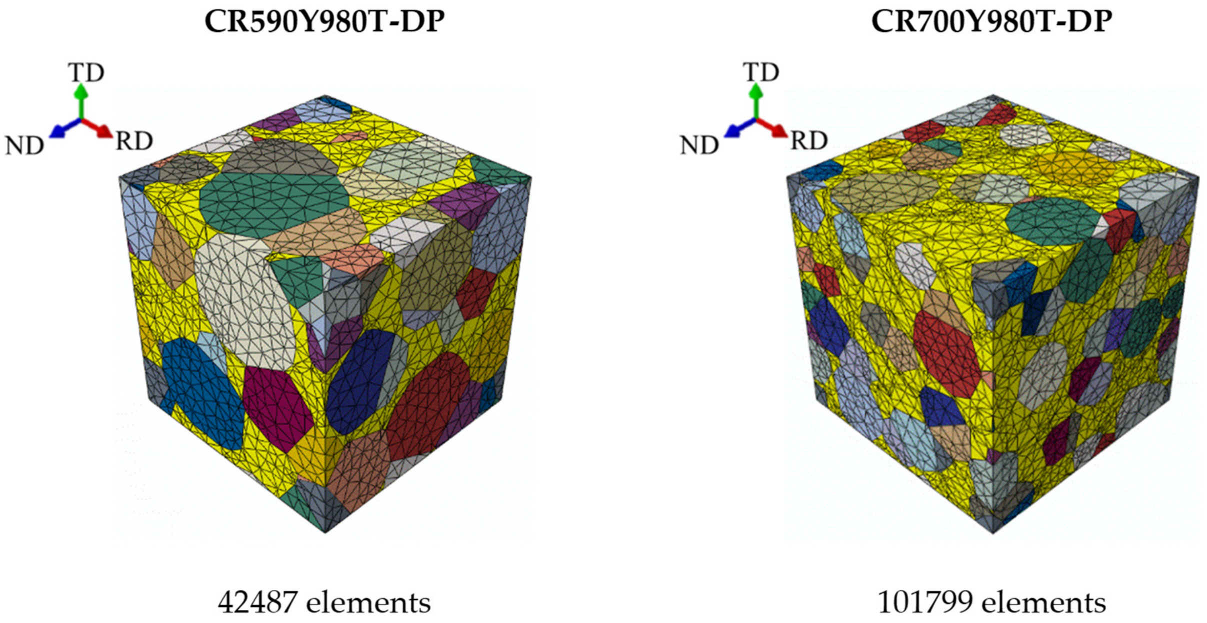

**Figure 14.** The meshing patterns of the different RVEs.

### 3.2. Deformation and Damage Assessments

The RVEs were constructed to study the grain-scale deformation and damage behaviors of the studied DP1000 steels under different loading conditions. This knowledge is vital in the material selection process, since some mechanical properties at the macroscopic scale are mainly dependent on the material microstructural features, such as the hole expansion ratio, which still remains a challenge in DP steels. Figures 15 and 16 illustrate the responses of the materials through different loading paths, uniaxial tension, equi-biaxial tension, plane strain tension, and pure shear. All the images were taken at an equivalent strain of 0.1 for the RVE boxes. The results show that although martensite represented higher level of stress, the contribution towards plastic deformation was mostly made by ferrite, since it is the softer phase, as also observed by Liu et al. [38]. A strong heterogeneous stress distribution was observed in CR590Y980T-DP, while the deformation partitioned very homogeneously in CR700Y980T-DP. This tendency was predictable in consideration of the more homogeneous and consistent microstructural and micromechanical features that were represented by CR700Y980T-DP, in terms of the phase fraction, grain size, texture, and mechanical properties of the different phases. Moreover, grain orientation influenced the different deformation contribution of each ferrite grain under different loading conditions. It is worth mentioning that the RVE of CR590Y980T-DP was strongly deformed under the shear condition, while no significant difference was seen for CR700Y980T-DP in comparison to the other loading paths.

Moreover, damage behavior of the RVEs were studied under various loading conditions, to compare the sensitivity of the materials through complicated local deformation, to estimate their capability of edge crack resistance. Note that an edge can experience severe shearing and uniaxial tension stress state at the cutting stage [5], and mixed uniaxial tension, plane strain, and biaxial tension during hole expansion tests [39]. The maximum shear stress at initiation of martensite cracking was obtained 1067 and 662 MPa for CR590Y980T-DP and CR700Y980T-DP, respectively. These values were derived from the calculated flow curve of martensite, Figure 12, at a plastic strain of 0.05, which assume martensite cracking initiates [35]. Based on the Tresca yield criterion, the maximum shear stress is half of the equivalent stress in uniaxial tensile test. The equivalent strain of the RVE box was calculated at the damage initiation moment (Figure 17). The results show that damage initiated in CR590Y980T-DP much earlier than that of CR700Y980T-DP, i.e., it is more sensitive to deformation. Therefore, it can be expected that CR590Y980T-DP is more prone to edge cracking and its HER is lower than CR700Y980T-DP, which was totally proved by the experimental results of hole expansion tests, Figure 18, where the HER of CR700Y980T-DP was 1.5 times that of CR590Y980T-DP. In brief, a lower strength differential between ferrite and martensite causes homogenous deformation and delays local damage initiation, which leads to higher edge crack resistance and a higher hole expansion ratio. This conclusion is supported by findings of other researchers from the microstructural analysis of other DP steels [16–18].

According to the RVE results (Figure 19), the ferrite–martensite interfaces represent the potential sites for damage initiation for both materials. However, the microstructural studies close to fracture site in uniaxial tensile specimens, Figure 20, reveal that the dominant damage micromechanism for CR590Y980T-DP was martensite cracking, while for CR700Y980T-DP, it was decohesion of the ferrite–martensite interfaces. It has been reported that fine microstructure in DP steels usually leads to a decohesion micromechanism, whereas coarser microstructure causes martensite cracking [37]. In fact, in both cases, the microcrack nucleates at the interfaces of the ferrite and martensite, and only its propagation path is different [40], which can also influence the multi-stage deformation processes, such as hole manufacturing and the subsequent hole expansion process. Nevertheless, damage propagation was not studied, as more factors should be considered in this regard, such as misorientation of neighbor grains. Marteau et al. [41] showed that the local microstructural neighborhood plays a more crucial role in strain heterogeneity rather than the specific grain orientation, shape, or size.

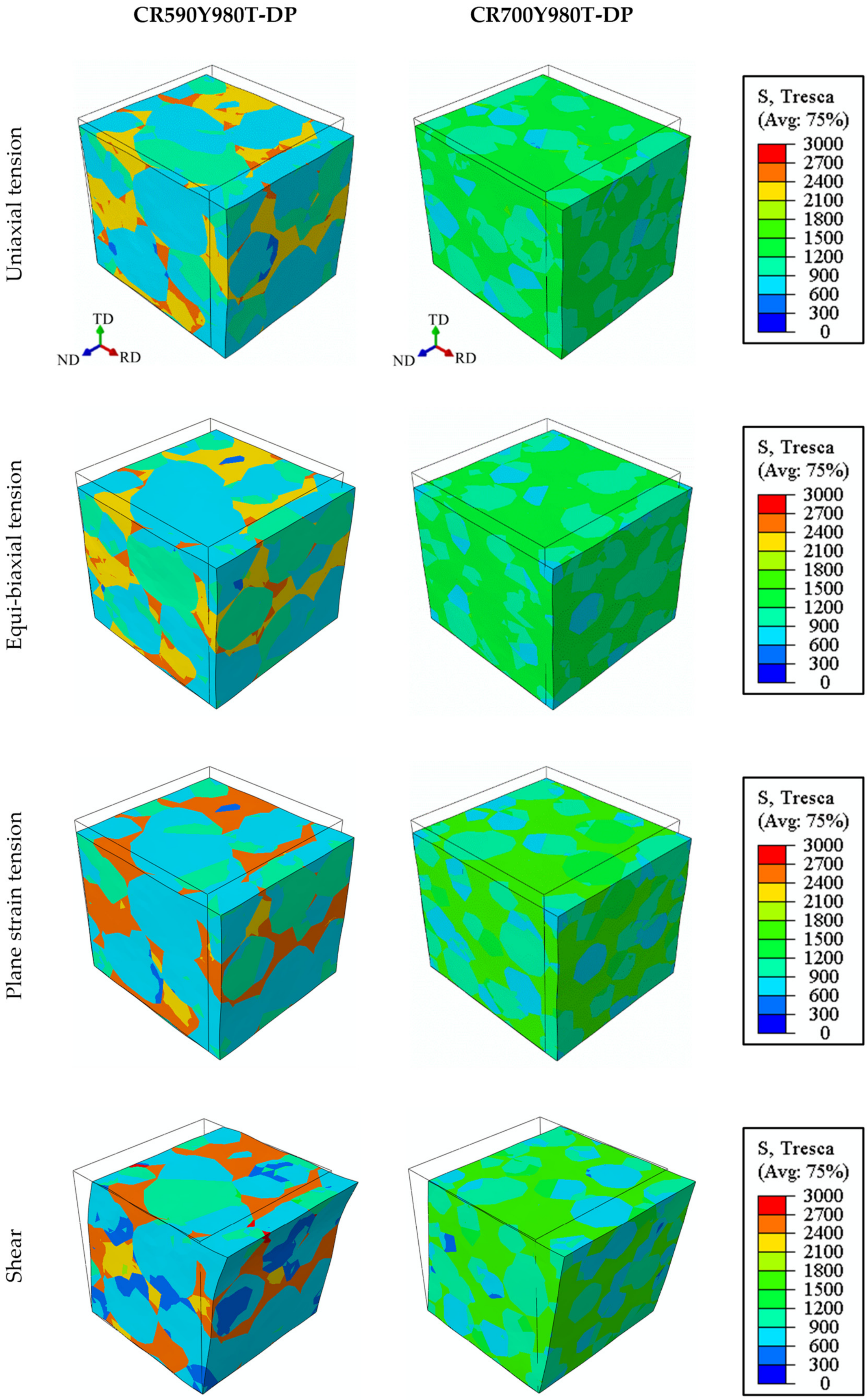

**Figure 15.** The responses of RVEs under different loading conditions, at an equivalent strain of 0.1 for the RVE box.

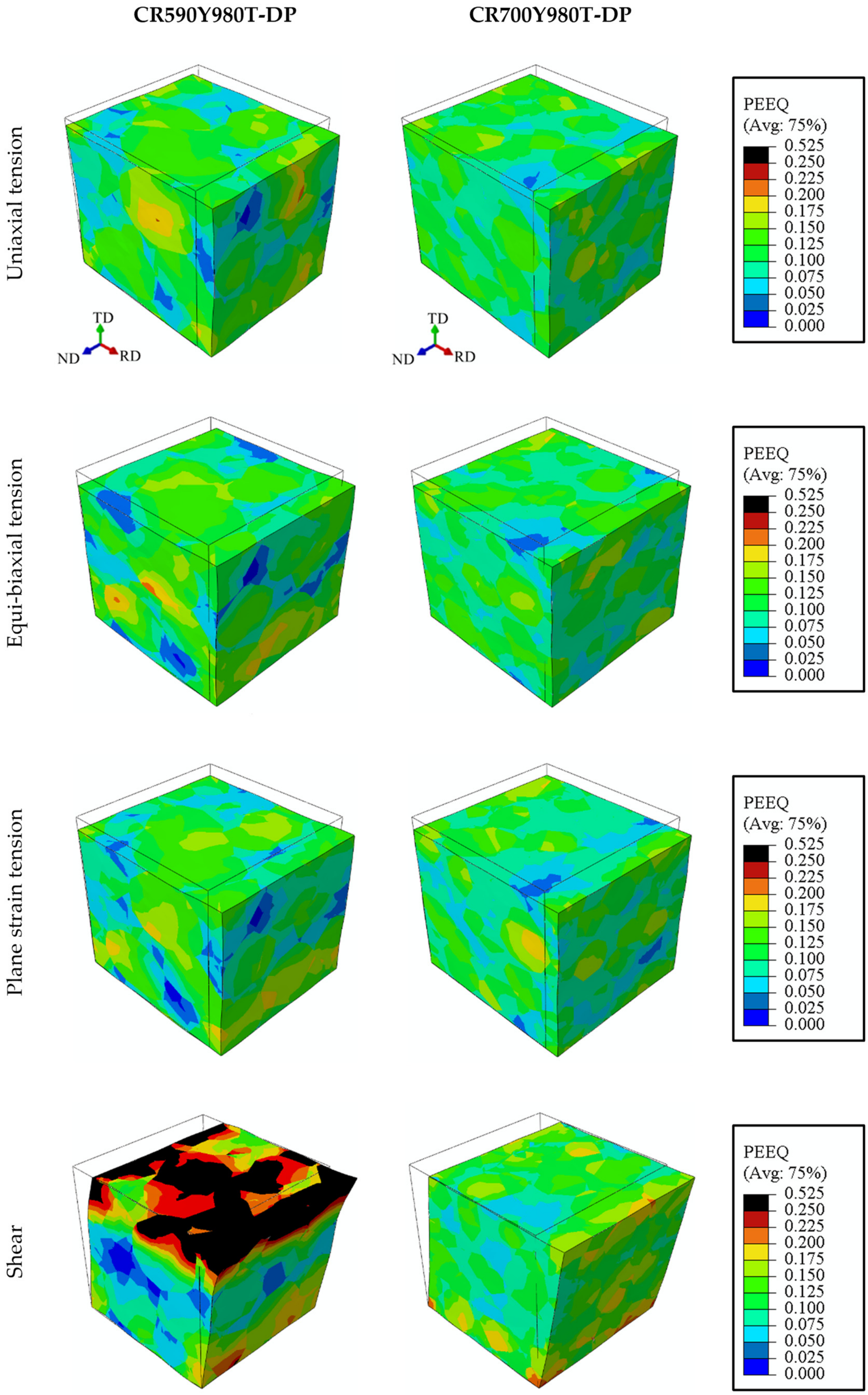

**Figure 16.** Strain partitioning of RVEs under different loading conditions, at an equivalent strain of 0.1 for the RVE box. "PEEQ" stands for equivalent plastic strain.

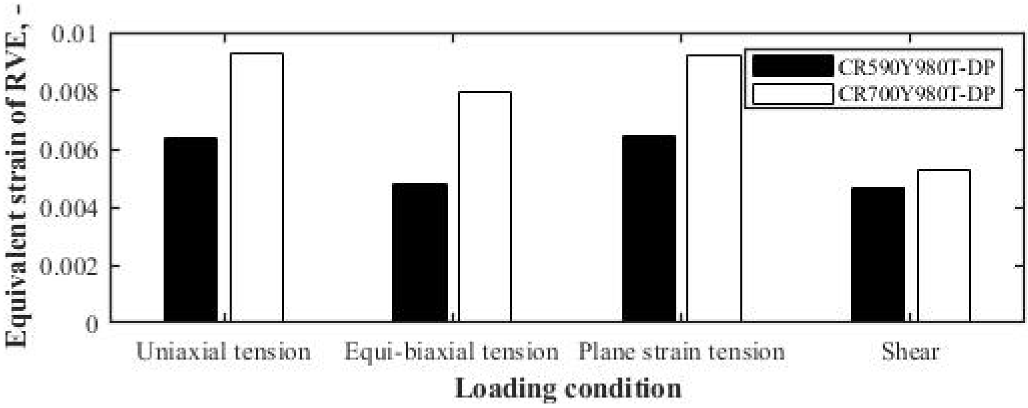

**Figure 17.** The predicted damage initiation of the RVEs at different loading conditions.

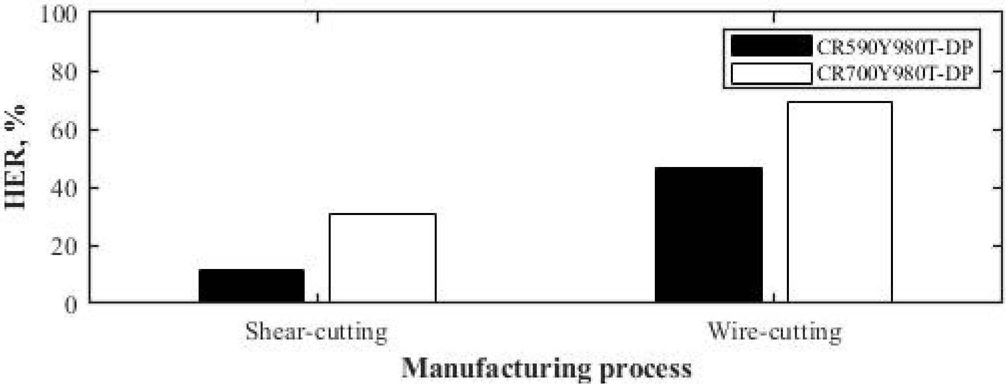

**Figure 18.** Comparison of hole expansion ratio and edge crack sensitivity of the studied materials.

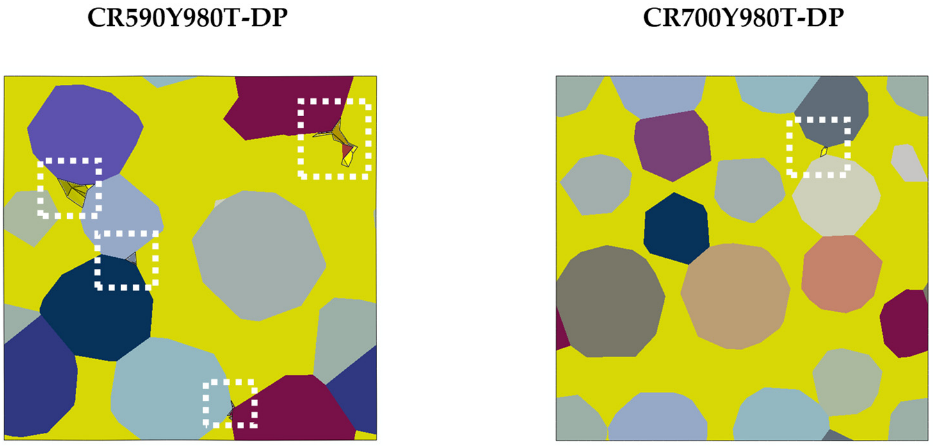

**Figure 19.** Some damage initiation sites are marked in cross-sections of the RVEs, which indicate damage initiates at the interfaces of the ferrite–martensite. The distribution of the phases is showed here. Martensite islands are shown in yellow, and the other colors illustrate the ferrite phases with different crystallographic orientations. The crack initiation was displayed by deletion of elements with the critical maximum shear stress.

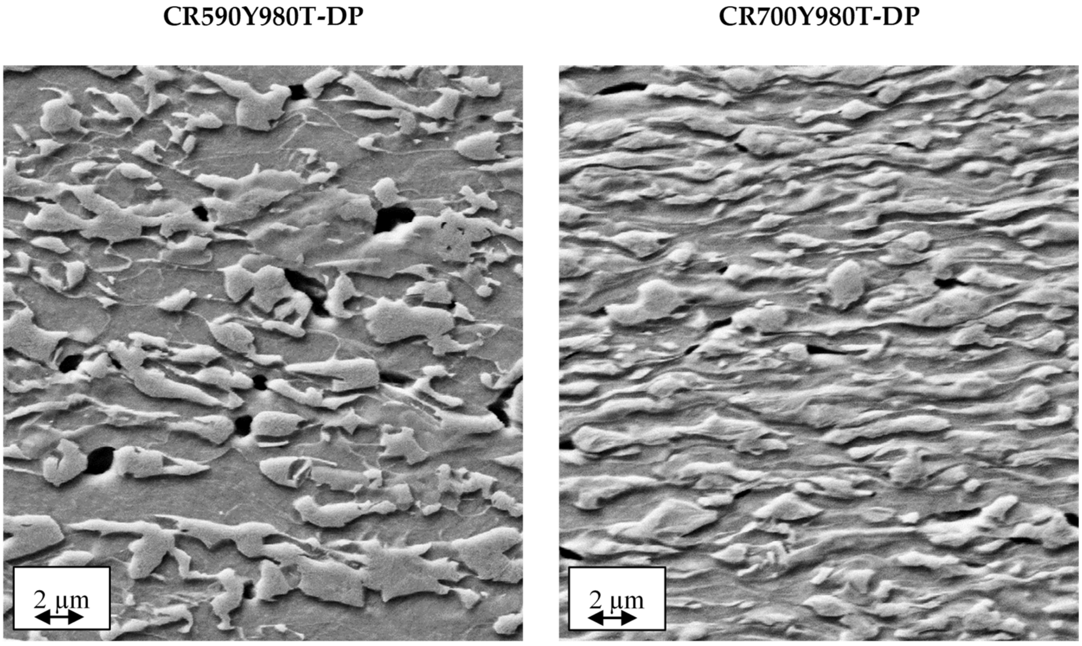

**Figure 20.** Martensite cracking and ferrite–martensite decohesion are observed in SEM images as the dominant damage micromechanisms in CR590Y980-DP and CR700Y980-DP, respectively.

## 4. Conclusions

Microstructure-based models of two DP1000 steels were generated using representative element methods according to the actual microstructural and micromechanical features of the materials. Damage initiation at the RVEs were evaluated for different loading conditions by using the maximum shear stress criterion to consider crack initiation in martensite. The results showed that when the microstructural and micromechanical properties of the ferrite and martensite were more similar, damage was triggered later; i.e., this material represented a higher local formability prior to damage initiation. Therefore, it is expected that edge crack sensitivity reduces and HER increases.

**Author Contributions:** Conceptualization, N.H. and S.M.; methodology, N.H. and S.M.; software, N.H. and N.V.; validation, N.H.; formal analysis, N.H.; investigation, N.H; writing—original draft preparation, N.H..; writing—review and editing, N.H., N.V. and S.M.; funding acquisition, S.M. All authors have read and agreed to the published version of the manuscript.

**Funding:** The funding of this research was provided by Deutsche Forschungsgemeinschaft (DFG, German Research Foundation)—Project number 278868966—TRR 188.

**Acknowledgments:** The authors would like to acknowledge Wenqi Liu and Junhe Lian from Aalto University for their support in the nanoindentation tests, and Seyed Amirhossein Motaman from RWTH Aachen University for his support in the texture analysis. In addition, the simulations were performed with computing resources granted by RWTH Aachen University under project <rwth0459>.

**Conflicts of Interest:** The authors declare no conflict of interest. The funders had no role in the design of the study; in the collection, analyses, or interpretation of data; in the writing of the manuscript, or in the decision to publish the results.

## References

1. Casellas, D.; Lara, A.; Frómeta, D.; Gutiérrez, D.; Molas, S.; Pérez, L.; Rehrl, J.; Suppan, C. Fracture toughness to understand stretch-flangeability and edge cracking resistance in AHSS. *Metall. Mater. Trans. A* **2017**, *48*, 86–94. [CrossRef]
2. Wu, X.; Bahmanpour, H.; Schmid, K. Characterization of mechanically sheared edges of dual phase steels. *J. Mater. Process. Technol.* **2012**, *212*, 1209–1224. [CrossRef]
3. Thakur, A.K.; Kumar, R.R.; Bansal, G.; Verma, R.K.; Tarafder, S.; Sivaprasad, S.; Mandal, G.K. Processing-microstructure-property correlation for producing stretch-flangeable grade dual-phase steel. *J. Mater. Eng. Perform.* **2021**, *30*, 4300–4317. [CrossRef]

4. Habibi, N.; Pütz, F.; Könemann, M.; Brinnel, V.; Münstermann, S.; Feistle, M.; Volk, W. Numerical quantification of damage accumulation resulting from blanking in multi-phase steel. *IOP Conf. Ser. Mater. Sci. Eng.* **2018**, *418*, 012058. [CrossRef]
5. Habibi, N.; Beier, T.; Richter, H.; Könemann, M.; Münstermann, S. The effects of shear affected zone on edge crack sensitivity in dual-phase steels. *IOP Conf. Ser. Mater. Sci. Eng.* **2019**, *651*, 012073. [CrossRef]
6. Butcher, C.; Anderson, D.; Worswick, M. Predicting failure during sheared edge stretching using a damage-based model for the shear-affected zone. *SAE Int. J. Mater. Manuf.* **2013**, *6*, 304–312. [CrossRef]
7. Levy, B.; Gibbs, M.; Van Tyne, C. Failure during sheared edge stretching of dual-phase steels. *Metall. Mater. Trans. A* **2013**, *44*, 3635–3648. [CrossRef]
8. Choi, S.-H.; Kim, E.-Y.; Woo, W.; Han, S.; Kwak, J. The effect of crystallographic orientation on the micromechanical deformation and failure behaviors of DP980 steel during uniaxial tension. *Int. J. Plast.* **2013**, *45*, 85–102. [CrossRef]
9. Tasan, C.C.; Diehl, M.; Yan, D.; Bechtold, M.; Roters, F.; Schemmann, L.; Zheng, C.; Peranio, N.; Ponge, D.; Koyama, M. An overview of dual-phase steels: Advances in microstructure-oriented processing and micromechanically guided design. *Annu. Rev. Mater. Res.* **2015**, *45*, 391–431. [CrossRef]
10. Pütz, F.; Shen, F.; Könemann, M.; Münstermann, S. The differences of damage initiation and accumulation of DP steels: A numerical and experimental analysis. *Int. J. Fract.* **2020**, *226*, 1–15. [CrossRef]
11. Ghadbeigi, H.; Pinna, C.; Celotto, S. Failure mechanisms in DP600 steel: Initiation, evolution and fracture. *Mater. Sci. Eng. A* **2013**, *588*, 420–431. [CrossRef]
12. Kusche, C.F.; Pütz, F.; Münstermann, S.; Al-Samman, T.; Korte-Kerzel, S. On the effect of strain and triaxiality on void evolution in a heterogeneous microstructure–A statistical and single void study of damage in DP800 steel. *Mater. Sci. Eng. A* **2021**, *799*, 140332. [CrossRef]
13. Ramazani, A.; Schwedt, A.; Aretz, A.; Prahl, U.; Bleck, W. Characterization and modelling of failure initiation in DP steel. *Comput. Mater. Sci.* **2013**, *75*, 35–44. [CrossRef]
14. Uthaisangsuk, V.; Prahl, U.; Bleck, W. Modelling of damage and failure in multiphase high strength DP and TRIP steels. *Eng. Fract. Mech.* **2011**, *78*, 469–486. [CrossRef]
15. Vajragupta, N.; Maassen, S.; Clausmeyer, T.; Brands, D.; Schröder, J.; Hartmaier, A. Micromechanical modeling of dp600 steel: From microstructure to the sheet metal forming process. *Procedia Manuf.* **2020**, *47*, 1540–1547. [CrossRef]
16. Pathak, N.; Butcher, C.; Worswick, M.J.; Bellhouse, E.; Gao, J. Damage evolution in complex-phase and dual-phase steels during edge stretching. *Materials* **2017**, *10*, 346. [CrossRef]
17. Fang, X.; Fan, Z.; Ralph, B.; Evans, P.; Underhill, R. Effects of tempering temperature on tensile and hole expansion properties of a C–Mn steel. *J. Mater. Process. Technol.* **2003**, *132*, 215–218. [CrossRef]
18. Hu, X.; Sun, X.; Raghavan, K.; Comstock, R.; Ren, Y. Linking constituent phase properties to ductility and edge stretchability of two DP 980 steels. *Mater. Sci. Eng. A* **2020**, *780*, 139176. [CrossRef]
19. Aurenhammer, F.; Klein, R. Voronoi Diagrams. *Handb. Comput. Geom.* **2000**, *5*, 201–290.
20. Bargmann, S.; Klusemann, B.; Markmann, J.; Schnabel, J.E.; Schneider, K.; Soyarslan, C.; Wilmers, J. Generation of 3D representative volume elements for heterogeneous materials: A review. *Prog. Mater. Sci.* **2018**, *96*, 322–384. [CrossRef]
21. Imai, H.; Iri, M.; Murota, K. Voronoi diagram in the Laguerre geometry and its applications. *SIAM J. Comput.* **1985**, *14*, 93–105. [CrossRef]
22. Vajragupta, N.; Wechsuwanmanee, P.; Lian, J.; Sharaf, M.; Münstermann, S.; Ma, A.; Hartmaier, A.; Bleck, W. The modeling scheme to evaluate the influence of microstructure features on microcrack formation of DP-steel: The artificial microstructure model and its application to predict the strain hardening behavior. *Comput. Mater. Sci.* **2014**, *94*, 198–213. [CrossRef]
23. Pütz, F.; Henrich, M.; Fehlemann, N.; Roth, A.; Münstermann, S. Generating input data for microstructure modelling: A deep learning approach using generative adversarial networks. *Materials* **2020**, *13*, 4236. [CrossRef]
24. Henrich, M.; Pütz, F.; Münstermann, S. A novel approach to discrete representative volume element automation and generation-DRAGen. *Materials* **2020**, *13*, 1887. [CrossRef] [PubMed]
25. Tarjus, G.; Schaaf, P.; Talbot, J. Random sequential addition: A distribution function approach. *J. Stat. Phys.* **1991**, *63*, 167–202. [CrossRef]
26. Torquato, S. Optimal design of heterogeneous materials. *Annu. Rev. Mater. Res.* **2010**, *40*, 101–129. [CrossRef]
27. Smit, R.J.; Brekelmans, W.M.; Meijer, H.E. Prediction of the mechanical behavior of nonlinear heterogeneous systems by multi-level finite element modeling. *Comput. Methods Appl. Mech. Eng.* **1998**, *155*, 181–192. [CrossRef]
28. Wu, W.; Owino, J.; Al-Ostaz, A.; Cai, L. Applying periodic boundary conditions in finite element analysis. In Proceedings of the SIMULIA Community Conference in Providence, Rhode Island, RI, USA, 20–22 May 2014; pp. 707–719.
29. Motaman, S.A.H.; Roters, F.; Haase, C. Anisotropic polycrystal plasticity due to microstructural heterogeneity: A multi-scale experimental and numerical study on additively manufactured metallic materials. *Acta Mater.* **2020**, *185*, 340–369. [CrossRef]
30. Motaman, S.A.H.; Haase, C. The microstructural effects on the mechanical response of polycrystals: A comparative experimental-numerical study on conventionally and additively manufactured metallic materials. *Int. J. Plast.* **2021**, *140*, 102941. [CrossRef]
31. Roters, F.; Eisenlohr, P.; Hantcherli, L.; Tjahjanto, D.D.; Bieler, T.R.; Raabe, D. Overview of constitutive laws, kinematics, homogenization and multiscale methods in crystal plasticity finite-element modeling: Theory, experiments, applications. *Acta Mater.* **2010**, *58*, 1152–1211. [CrossRef]

32. Rice, J.R. Inelastic constitutive relations for solids: An internal-variable theory and its application to metal plasticity. *J. Mech. Phys. Solids* **1971**, *19*, 433–455. [CrossRef]
33. Tasan, C.C.; Diehl, M.; Yan, D.; Zambaldi, C.; Shanthraj, P.; Roters, F.; Raabe, D. Integrated experimental–simulation analysis of stress and strain partitioning in multiphase alloys. *Acta Mater.* **2014**, *81*, 386–400. [CrossRef]
34. Sung, J.H.; Kim, J.H.; Wagoner, R. A plastic constitutive equation incorporating strain, strain-rate, and temperature. *Int. J. Plast.* **2010**, *26*, 1746–1771. [CrossRef]
35. Steinbrunner, D.L.; Matlock, D.; Krauss, G. Void formation during tensile testing of dual phase steels. *Metall. Trans. A* **1988**, *19*, 579–589. [CrossRef]
36. Digimizer, image analysis software; MedCalc Software Ltd., Ostend, Belgium. Available online: https://www.digimizer.com (accessed on 23 March 2021).
37. Tasan, C.C.; Hoefnagels, J.P.; Diehl, M.; Yan, D.; Roters, F.; Raabe, D. Strain localization and damage in dual phase steels investigated by coupled in-situ deformation experiments and crystal plasticity simulations. *Int. J. Plast.* **2014**, *63*, 198–210. [CrossRef]
38. Liu, W.; Lian, J.; Aravas, N.; Münstermann, S. A strategy for synthetic microstructure generation and crystal plasticity parameter calibration of fine-grain-structured dual-phase steel. *Int. J. Plast.* **2020**, *126*, 102614. [CrossRef]
39. Paul, S.K. A critical review on hole expansion ratio. *Materialia* **2020**, *9*, 100566. [CrossRef]
40. Alharbi, K.; Ghadbeigi, H.; Efthymiadis, P.; Zanganeh, M.; Celotto, S.; Dashwood, R.; Pinna, C. Damage in dual phase steel DP1000 investigated using digital image correlation and microstructure simulation. *Model. Simul. Mater. Sci. Eng.* **2015**, *23*, 085005. [CrossRef]
41. Marteau, J.; Haddadi, H.; Bouvier, S. Investigation of strain heterogeneities between grains in ferritic and ferritic-martensitic steels. *Exp. Mech.* **2013**, *53*, 427–439. [CrossRef]